Effect of SiC Deposition Behavior on Microstructure and Mechanical Properties of Cold-Sprayed Al5056/SiC Composite Coatings

Hongyu Zhang[1] · Min Yu[1] · Chunming Liang[1] · Hui Chen[1]

Abstract To study the effect of deposition behavior of the reinforcement on microstructure and property of cold-sprayed metal matrix composite coating, four Al5056 composite powders containing 15 wt.%, 30 wt.%, 45 wt.% and 60 wt.% SiC were mixed to prepare the composite coatings by cold spraying. Effect of the SiC deposition behavior on microstructure, SiC distribution, micro-/nanohardness, surface residual stress and shear strength of the coatings were studied. Experimental results show that the increase in SiC content in the powder increased the SiC collision with the deposited SiC particles, which caused the difference in SiC content and distribution in the composite coatings. The SiC deposition behavior caused the SiC morphology to evolve from integrity to small cracks and complete fragmentation. The SiC deposition behavior effectively influenced its peening effect on the deformed Al5056 particles, that is, as the SiC fragmentation threshold arrived, the nanohardness, surface residual stress and shear strength of the coating showed the corresponding transition point. The surface residual stress state of the deformed Al5056 matrix could in turn affect the SiC deposition by increasing the SiC deposition efficiency at the minimum compressive stress.

Keywords Al5056 · SiC composite coating · cold spray · mechanical properties · residual stress · SiC fragmentation

✉ Min Yu
yumin@home.swjtu.edu.cn

1 Research center of Sichuan Advanced Welding and Surface Engineering, School of Materials Science and Engineering, Southwest Jiaotong University, Chengdu 610063, People's Republic of China

Introduction

Cold spray (CS) is a rapidly developing spraying technique, in which supersonic gas jets accelerate solid particles to a high velocity (500–1000 m/s) and deposit a coating at a temperature far below the solid particle melting point (Ref 1, 2). The low-temperature deposition protects the particles from oxidation and phase transformation, which makes it particularly suitable for thermal sensitive materials (Ref 3). Particles undergo large plastic deformations with high strain rates up to 10^9 s^{-1} as impacting the substrate, which generally results in a significant compressive residual stress (Ref 4-7). The distinct features of CS in terms of low-temperature deposition and the compressive residual stress provide its remarkable applications in repair (Ref 8-10) and solid-state additive manufacturing (Ref 8, 11-13).

CS is a feasible method for preparing a metal-matrix composite (MMC) coating that is composed of a highly deformed matrix and non-deformed reinforcements (Ref 14-21). The addition of the reinforcements usually improves the coating deposition efficiency (Ref 22) and mechanical and physical properties through work-hardening, dispersion strengthening and grain refinement (Ref 18). The hardness of cold-sprayed Al coatings can be improved by incorporating micro-sized ceramic powders of SiC, B$_4$C, TiN and Al$_2$O$_3$ (Ref 14, 20, 23). The main reinforcing principle is attributed to the severe plastic deformation of the Al matrix because of the compaction of the hard ceramics. Ceramic particles restrict further deformation of the soft Al matrix during loading (Ref 24). Although the same Al matrix is used, the difference in elastic modulus and particle size of the ceramic powders produces different reinforcement effects. According to Meydanoglu et al.(Ref 25) the wear performance of the

7075Al composite coating that is reinforced with B_4C powder is better than that of the coating reinforced with the SiC powder. The B_4C particles in the coating promote strain localization during reciprocating sliding and produce a third-body microstructure that is more uniform than the SiC particles, which protects the underlying Al matrix from deformation. For the same Al_2O_3 powder, the spherical morphology shows a superior wear resistance compared to the angular morphology with a similar Al_2O_3 content in the coating (Ref 26, 27).

Generally, the non-deformed reinforcements can only be co-deposited in the composite coatings by peening and mechanical wedging into the deposited matrix or by being embedded by the incoming "soft" matrix (Ref 28). The peening and wedging actions of the reinforcements may cause further plastic deformation of the matrix (Ref 14, 18, 29), which could increase the residual stress in the cold-sprayed composite coatings.

From a structural integrity perspective, many physical properties, such as the fatigue life and wear resistance, are intrinsically linked to the surface residual stress state. Therefore, besides the influence of inherent characteristics of the ceramic on the coating performance, an investigation into the effect of deposition behavior of the reinforcements on the microstructure and residual stress of the composite coatings could provide additional understanding of the strengthening mechanism of the reinforcements in cold-sprayed composite coatings.

Material and method

Material

Commercial Al5056 and SiC (Beijing United Coating technologies Co., Ltd, China) powders were used as the matrix and reinforcement, respectively. Morphology and particle size distribution of the powders are shown in Fig. 1. The Al5056 powder shows a spherical morphology with an average diameter of 24.6 μm. The SiC powder shows an irregular morphology with an average particle size of 13.6 μm. The pure Al plates were used as substrate and sand-blasted using alumina grits (147 μm) at a pressure of 0.2 MPa before spraying.

Coating Preparation

The Al5056 powder was mechanically mixed with the SiC powder to prepare composite powders, having SiC mass fractions of 15, 30, 45 and 60 wt.%, equivalent to 12.7, 26.1, 40.3 and 55.3 vol.%. Al5056/SiC composite coatings were prepared using a cold spray system, which was assembled and built by Northwestern Polytechnical University. The nozzle has an expansion ratio of 6.7 and a divergent section length of 200 mm. High-pressure nitrogen gas was used as the driving gas with a pressure of 2.6 MPa and temperature of 673 K. Argon was used as the powder carrier gas with a pressure of 2.8 MPa, and the powder was axially fed into the nozzle. The standoff distance from the nozzle exit to substrate was set to 30 mm.

Characterization Procedures

Microstructure

The cross-sectional microstructures of the coatings were observed using an optical microscope (AX10) and scanning electron microscope (SEM, JSM 5800LV, JEOL, Japan) including energy dispersive x-ray spectroscopy (EDS). The SiC content in the composite coatings was determined by image analysis with Image Pro Plus software using ten metallographic images.

Distribution of SiC

Box dimension method (Ref 29-33) based on the fractal theory was used to estimate the uniformity of SiC distribution in the coatings. The detailed information can be found in the literature (Ref 33). The image analysis was also used to obtain SiC distribution information, and nine cross-sectional metallographic images at 200 magnification were used. Figure 2 shows one representative image, where R is the equivalent length of the square, r_i ($i=1,2,3,...n$) is the distance from the i-th particle to the center point O, N is the number of SiC particle in the square, and D is the actual dimension value of the cold-sprayed coatings, which is reciprocal of the formula slope based on the following equations:

$$R(N) = \left(\frac{1}{N}\sum_{i=1}^{N} r_i^2\right)^{\frac{1}{2}} \tag{Eq 1}$$

$$\ln R_g = \frac{1}{D}\ln N + \ln K \tag{Eq 2}$$

In the case of the two-dimensional metallographic image, the dimension value D should be compared with the ideal dimension value 2, and the relative deviation value σ ($\sigma=|D-2|/2$) is the quantitative factor of SiC distribution uniformity in the coating, i.e., the smaller the σ is, the better the uniformity is.

Hardness

A digital microhardness tester (HXD-1000TM, Shanghai optical instruments Co, Ltd., China) was used to measure the Vickers hardness of the coatings. The loading force was
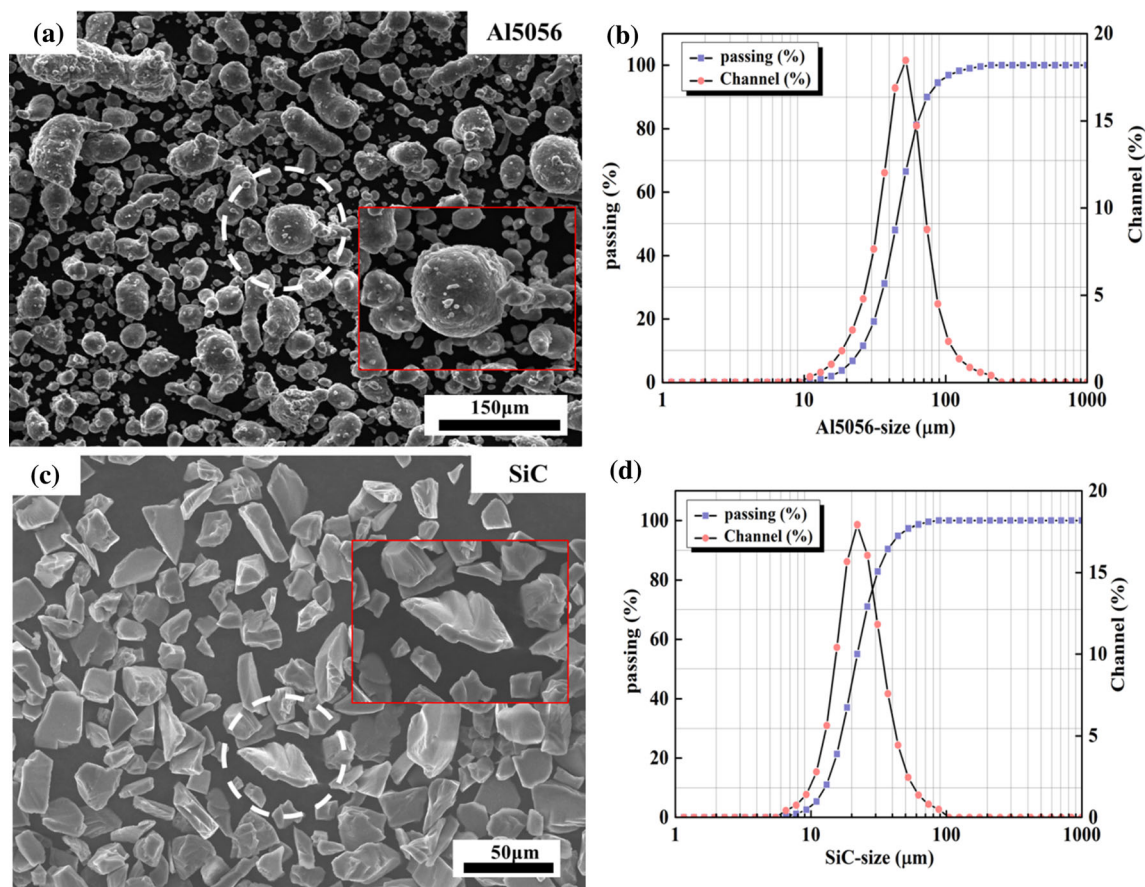
Fig. 1 SEM morphologies of the used powders (a) Al 5056 and (c) SiC, and powder size distribution of (b) Al 5056 and (d) SiC
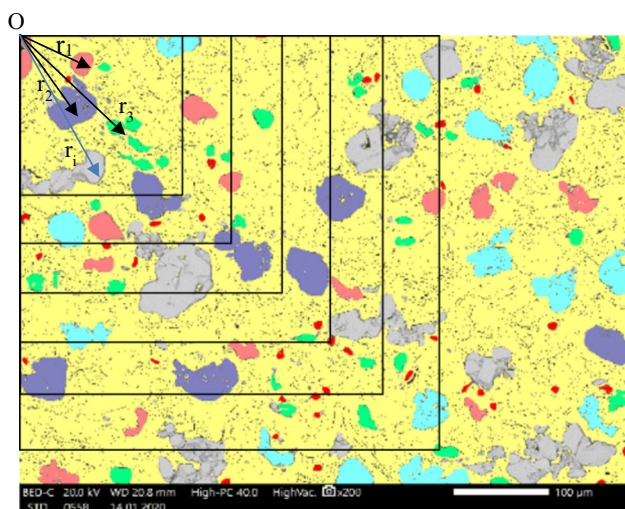
Fig. 2 Selection diagram of SiC particles for box dimension method

0.2 kg with a holding time of 10 s. Nanoindentation measurements were carried out on the deformed Al5056 matrix in the composite coatings with a typical diamond Berkovich indenter (Agilent Nano Indenter G200, America). In depth control nanoindentation method with constant depth

of 1500 nm was used, and nanohardness was calculated based on the model of Oliver-Pharr approach, which can be executed from the software provided by the G200 instrument. The average nanohardness was determined based on five Al5056 matrix micro-zones at the middle cross-sectional coating.

Residual Stress Measurement

The x-ray diffraction analysis system (Empyrean, PANalytical B.V.) was used to measure the residual stress of the coating surface. Its measurement principle is based on the $sin^2\psi$ method. Bragg's equation (Eq3) was used to describe the relationship between the original diffraction angle θ and the lattice distance d,

$$2d \sin\theta = n\lambda \qquad (Eq\ 3)$$

Where, λ is the X-ray wavelength and n is the diffraction order.

When X-rays are irradiated on the crystals with residual stress, the strain and lattice distance in different orientation (ψ) would change. The strain can be calculated as,

$$\varepsilon_{\phi\psi} = \frac{d_{\phi\psi} - d_\circ}{d_\circ} = \frac{\Delta d}{d_\circ} \tag{Eq 4}$$

where $\varepsilon_{\phi\psi}$ is the strain of polycrystals, $d_\circ$ is the plane spacing without stress, $d_{\phi\psi}$ is the plane spacing with stress.

According to the theory of elasticity, as for a continuous, homogeneous and isotropic object, the strain $\varepsilon_{\phi\psi}$ in any direction can be expressed as,

$$\varepsilon_{\phi\psi} = \alpha_1^2 \varepsilon_1 + \alpha_2^2 \varepsilon_2 + \alpha_3^2 \varepsilon_3 \tag{Eq 5}$$

where , $\alpha_1, \alpha_2, \alpha_3$ are the directional cosine of $\varepsilon_{\phi\psi}$ relative to O-XYZ coordinate system.

Deriving $\varepsilon_{\phi\psi}$ from $\sin^2 \psi$ under the plane stress state ($\sigma_z = 0$, $\varepsilon_z = \varepsilon$),

$$\sigma_\phi = \frac{E}{1+v} \frac{\partial \varepsilon_{\phi\psi}}{\partial \sin^2 \psi} \tag{Eq 6}$$

By combining Eq 4 with deriving $\sin^2 \psi$,

$$\frac{\partial \varepsilon_{\phi\psi}}{\partial \sin^2 \psi} = -\frac{\cot \theta_\circ}{2} \frac{\partial 2\theta_{\phi\psi}}{\partial \sin^2 \psi} \tag{Eq 7}$$

By combining Eqs 6 and 7 can get a practical equation as follows,

$$\sigma_\phi = -\frac{E}{2(1+v)} \cot \theta_\circ \frac{\pi}{180°} \frac{\Delta 2\theta_{\phi\psi}}{\Delta \sin^2 \psi} \tag{Eq 8}$$

Defining

$$K = -\frac{E}{2(1+v)} \cot \theta_\circ \frac{\pi}{180°} \tag{Eq 9}$$

$$M = \frac{\Delta 2\theta_{\phi\psi}}{\Delta \sin^2 \psi} \tag{Eq 10}$$

Then the residual stress σ_ϕ can be calculated as,

$$\sigma_\phi = KM \tag{Eq 11}$$

where K is a stress constant related to the elastic modulus, E is Young' modulus, v is Poisson's ratio. M is the slope of a 2 $\theta_{\phi\psi}$-$sin^2\psi$ straight line.

The test parameters are listed in Table 1. The different diffraction angle 2θ and corresponding $sin^2\psi$ is measured by selecting different tilt angles ψ (0°, 18.43°, 26.57°,

Table 1 $sin^2 \psi$ test parameters

Parameter	Value
Tube current	40 mA
Tube voltages	40 KV
Target	Cu-Kα
Scanning speed	0.04–0.02°/S
Diffraction lattice ($h\,k\,l$)	Al (311)
Wavelength (Cu-Kα)	1.540598 (Å)

33.21°, 39.23°, 45°). The elastic modulus and Poisson's ratio of Al (311) crystal plane is 70.14 GPa and 0.3499, respectively.

Shear Strength

The shear strength of the coating and substrate was tested using a microcomputer control electronic universal testing machine (CMT4304, Shanghai Jiehu Instruments Co., Ltd, China) at a speed of 0.5 mm/min. Figure 3a shows a schematic diagram of the shear test, and Fig. 3b shows dimensions of the shear test specimens.

Results and Discussion

Coatings Microstructure

The cross-sectional morphology of the cold-sprayed Al5056/SiC composite coating is shown in Fig. 4. The composite coating is composed of extensively deformed Al5056 particles and non-deformed SiC particles. The SiC particles were deposited preferentially at the corners that were formed by the deposited Al5056 particles and covered by the subsequent Al5056 particles, as shown in Fig. 4(a). As the SiC content in the sprayed powders increased from 15 wt.% to 30 wt.%, some cracks in the SiC particles are observed in Fig. 4(b). With a further increase to 45 wt.%, the SiC particles were broken severely but maintained the complete particle morphology in Fig. 4(c). The composite coating was covered by small broken SiC particles up to 60 wt.%, as shown in Fig. 4(d). Figure 5 shows the retained SiC content in the coating as a function of its content in the powder. The average SiC content in the composite coatings increased from 12.7 vol.%, 17 vol.%, 22.8 vol.% to 31.9 vol.% as the SiC content in the powders increased from
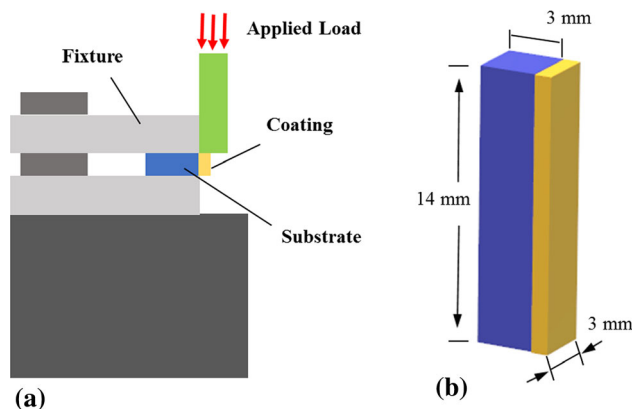
Fig. 3 (a) Schematic diagrams of the shear test and (b) dimension of the specimens

Fig. 4 Microstructures of cold-sprayed composite coatings of (a) Al5056+15 wt.%SiC, (b) Al5056+30 wt.%SiC, (c) Al5056+45 wt.%SiC and (d) Al5056+60 wt.%SiC. Note that figures (a-1)(a-2) ∼(d-1)(d-2) are enlarged views of (a∼d)
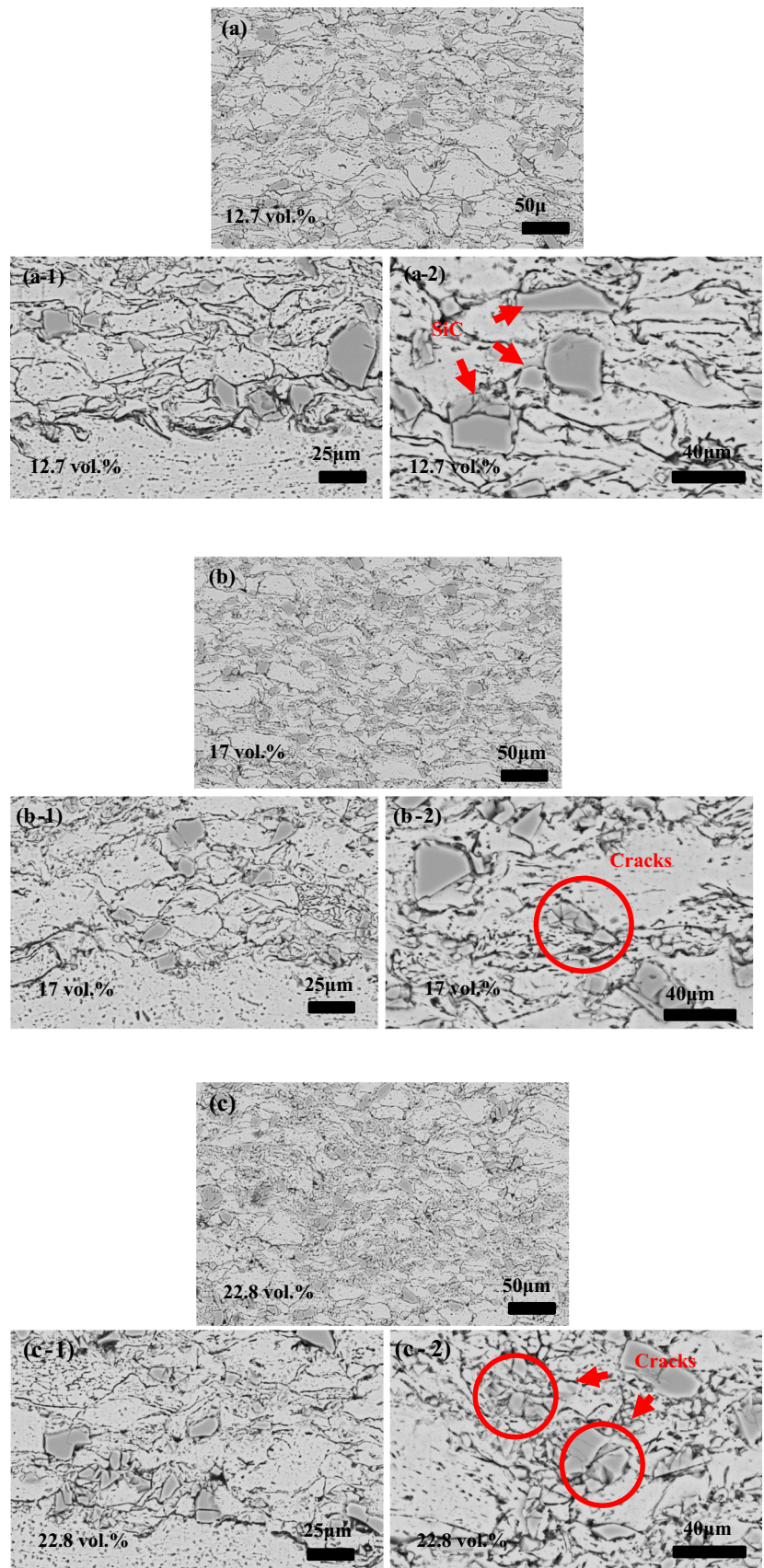
Fig. 4 continued

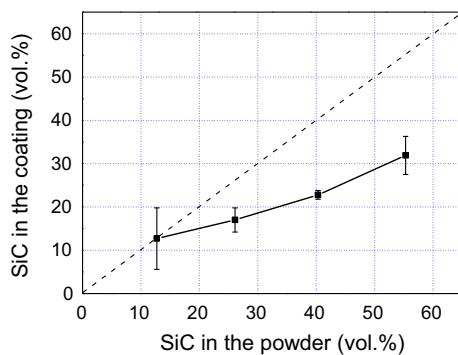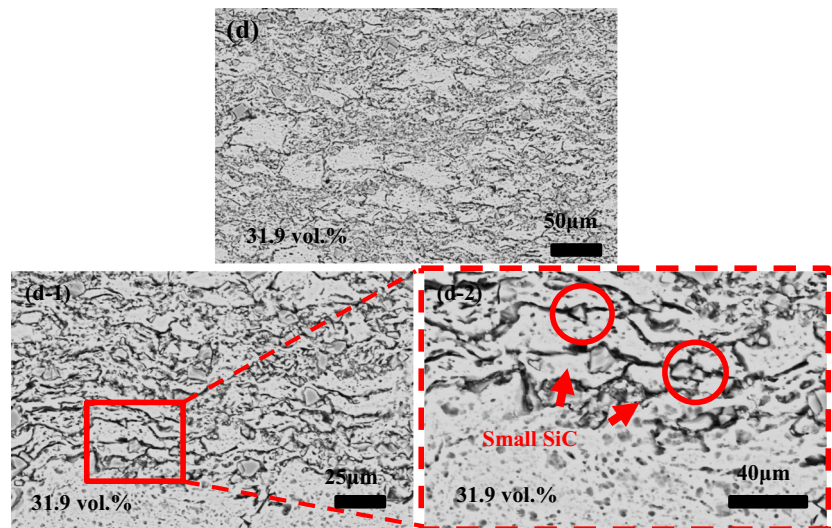Evolution of SiC content in the coating with the powder

Fig. 5 Evolution of SiC content in the coating with the powder

12.7 vol.%, 26.1 vol.%, 40.3 vol.% to 55.3vol.%, respectively.

The content loss and fragmentation of the hard SiC particles in the cold-sprayed Al composite coatings were reported by Sansoucy (Ref 16) and Yu (Ref 20). SiC particles are thought to impact deposited particles, and cause fragmentation, rebound and loss during the deposition (Ref 22, 34). When Al+12.7 vol.% ~40.3 vol.% SiC composite powders were sprayed, the 14 vol.% SiC increase in the powder only caused a 5 vol.% increase in the coating with an increased collision probability of the subsequent SiC particles on the deposited particles and fragmentation initiation of the SiC particles. With an increase in SiC content in the powder to 55.3 vol.%, the SiC deposition caused a ~9 vol.% increase in the coating. The results suggest that the SiC particle fragmentation facilitates its deposition in the coating.

SiC Distribution in Composite Coating

Figure 6 shows the $\ln(R)$–$\ln(N)$ fitting curves of the cold-sprayed composite coatings. The fitting parameters are shown in Table 2. The coefficient R^2 of the four composite coatings is close to 1, which suggests a good fit with the experimental data. The relative deviation value σ of the Al5056/17 vol.% SiC coating was smallest at 0.261%, whereas the maximum relative deviation value σ of the Al5056/12.7 vol.% SiC coating was 9.86%. A smaller relative deviation value suggests a better uniformity, thus the SiC distribution uniformity of the four Al5056/SiC composite coatings can be ranked: Al5056/17 vol.%SiC > Al5056/22.8 vol.%SiC > Al5056/31.9 vol.%SiC > Al5056/12.7 vol.%SiC.

Previous cold-sprayed Al5056/SiC-67 composite coatings (Ref 33) had an average Al5056 and SiC powder particle size of 20 μm and 67 μm, respectively. The effect of SiC particle size on the relative deviation σ is shown in Fig. 7. The relative deviation value σ of the Al5056/SiC-13.6 composite coating is smaller than that of the Al5056/SiC-67 composite coating, which indicates that the smaller SiC powder has a positive effect on the uniform distribution in the composite coatings.
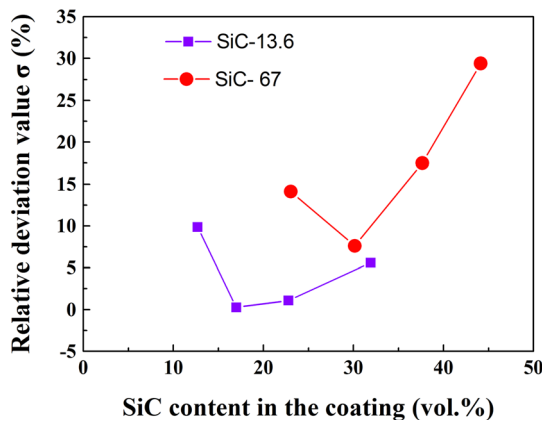
Coating Hardness

Figure 8 shows the evolution of coating microhardness with SiC content in the coating. The average microhardness of the cold-sprayed Al5056/SiC composite coatings was ~108, 114, 116 and 133 HV, which corresponds to the SiC content of 12.7 vol.%, 17 vol.%, 22.8 vol.% and 31.9 vol.% in the coating. An increase in SiC content in the coating increases the coating hardness. Ceramic particles can limit further deformation of the soft Al matrix and allow the load to be shared with the matrix during loading (Ref 24). The general hardness tendency does not explain the slight hardness increase with increase in SiC content increases from 17 vol.% to 22.8 vol.% in the coating. Besides the

Fig. 6 Ln(R)-ln(N) fitting
curves of cold-sprayed
composite coatings of
(a) Al5056/12.7 vol.%SiC,
(b)Al5056/17 vol.%SiC,
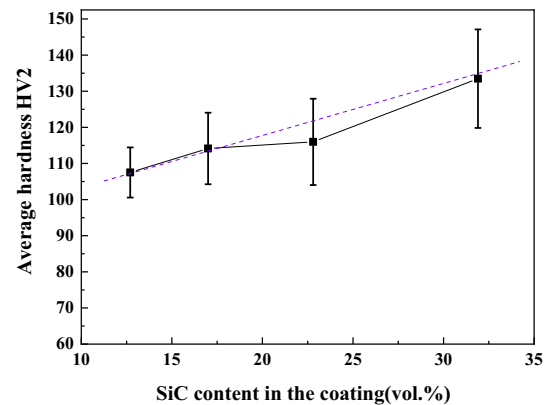(c) Al5056/22.8 vol.%SiC and
(d) Al5056/31.9 vol.%SiC
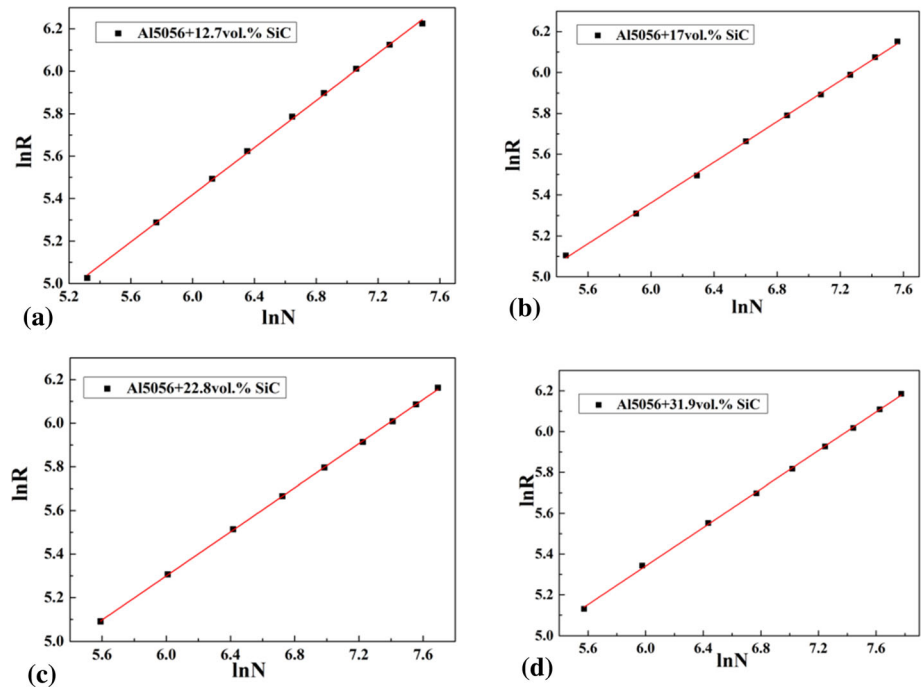
Table 2 Box dimension method parameters of the cold-sprayed Al5056/SiC coating

Coatings	Fitting equation	R^2	$\sigma\%$
Al5056+12.7 vol.%SiC	$\ln R = 0.5547 \ln N + 2.0907$	0.9992	9.86
Al5056+17 vol.%SiC	$\ln R = 0.4987 \ln N + 2.3697$	0.9995	0.261
Al5056+22.8 vol.%SiC	$\ln R = 0.5056 \ln N + 2.2659$	0.9999	1.11
Al5056+31.9 vol.%SiC	$\ln R = 0.472 \ln N + 2.5092$	0.9995	5.59

Fig. 8 Evolution of microhardness of the composite coatings with SiC content in the coating

Fig. 7 Comparison on relative deviation value of Al5056/SiC-13.6 with Al5056/SiC-67 composite coating

effect of SiC content in the coating on the microhardness, the combined effect of a weakening load of the broken SiC particles and strengthened load of the severer plastic deformation of the Al5056 particles affects the coating microhardness.

To quantify the effect of Al5056 deformation on hardness, only the deformed Al5056 particles were tested by the nanoindentation tests. Figure 9(a) shows the representative load–displacement curve of the four composite coatings at a fixed indentation depth of 1500 nm, and Fig. 9(b) shows the average nanohardness of the Al5056 matrix. The average nanohardness was 1.203, 1.292, 1.079 and 1.18 GPa for the Al5056/12.7 vol.% SiC, Al5056/17 vol.% SiC, Al5056/22.8 vol.% SiC and Al5056/31.9 vol.% SiC, respectively. The error bars in Fig. 9(b) show that the average nanohardness of the four composite coatings was similar because of the inhomogeneous deformation of the Al matrix from the difference in Al5056 particle size and
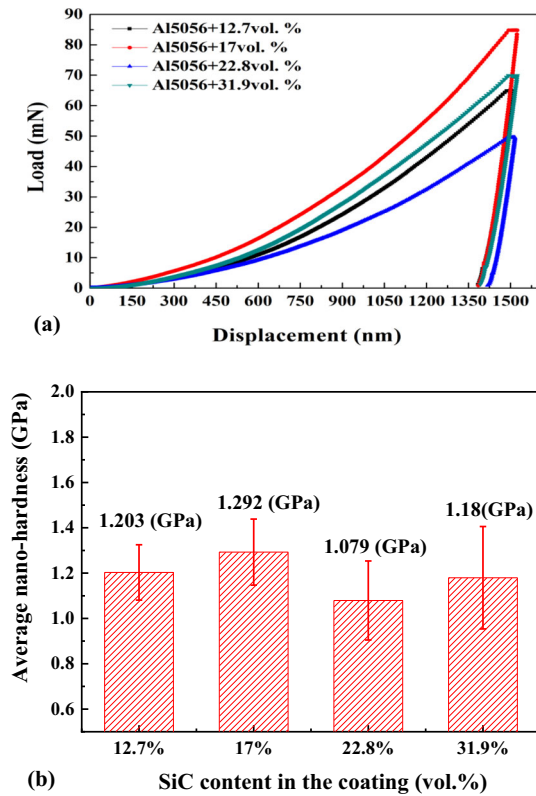
Fig. 9 (a) Load–displacement curves and (b) average nanohardness of cold-sprayed Al5056/SiC composite coatings

SiC peening effect. A comparison of the nanohardness and microhardness of the composite coatings shows that the increase in microhardness could result mainly because of the SiC load sharing.

Coating Shear Strength

Figure 10 shows the effect of SiC content in the coating on the shear strength of the coating with the substrate. As the SiC content in the coating increased from 12.7 vol.% to 17 vol.%, the average shear strength of the composite coating increased from 55.13 MPa to 57.96 MPa and peaked at ∼62.65 MPa with 22.8 vol.% SiC in the coating. As the SiC content in the coating increased to 31.9 vol.%, the shear strength decreased to 59.14 MPa.

To explore the adhesion characteristics of the coating with the substrate, the shear fracture morphology was observed and is shown in Fig. 11. Figure 11(a) shows the shear fracture morphology of the substrate. The interfacial fracture of the substrate side was flat, and elemental oxygen that was detected from EDS analysis may have resulted from oxidation of the fresh Al substrate after sandblasting. Figures 11(b)–(e) show the shear fracture morphologies of the composite coating sides. The fracture model of the composite coatings showed the same spalling pattern,
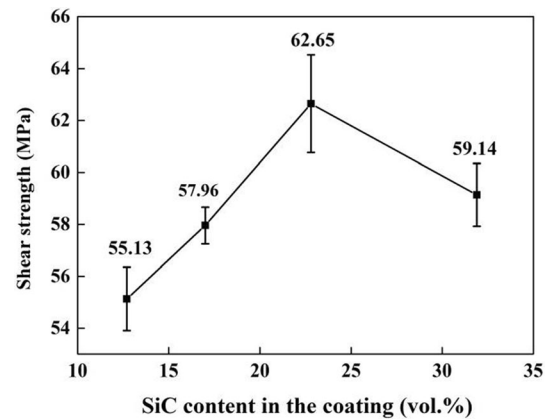
Fig. 10 Effect of SiC content in the coating on shear strength of the composite coatings

which indicates that the mechanical interlocking bonding of the deformed Al5056 splats contributed mainly to the shear strength. Therefore, the strength depends on the Al5056 particles deformation and the reduction in effective load area, which depends on the content, distribution and fragmentation of the SiC particles, that is, the SiC deposition behavior. As the SiC content in the coating increased from 12.7 vol.% to 22.8 vol.%, the reinforced Al5056 particle deformation increased the bonding strength. An increase to 31.9 vol.% with complete fragmentation of SiC particles in the coating decreased the effective load area, and cracks in the SiC particles decreased the bonding strength, which resulted in a reduction in shear strength.

Quantitative Analysis of Residual Stress

The residual stress of the surface Al5056 coating was measured by the $sin^2\psi$ method. Figure 12 shows the fitting plots of $2\theta_{\phi\psi}$-$sin^2\psi$ for the coatings, and the calculated residual stress is shown in Fig.13. The average surface residual stress of the Al5056 matrix that was reinforced with 12.7 vol.% SiC was -38.3 MPa, and as the SiC content in the coating increased to 17 vol.%, the residual stress increased to -47.3 MPa. As the SiC content increased to 22.8 vol.%, the residual stress decreased to -23.9 MPa, and with a further increase in SiC content to 31.9 vol.%, the residual stress slightly increased to − 32.2 MPa.

Discussion

The residual stress in cold-sprayed coatings has been reported as a compressive stress with magnitudes from − 20 to − 100 MPa (Ref 4, 36, 37). The peening effect on deposition caused a compressive stress at the coating surface. The limited penetration depth of the X-rays
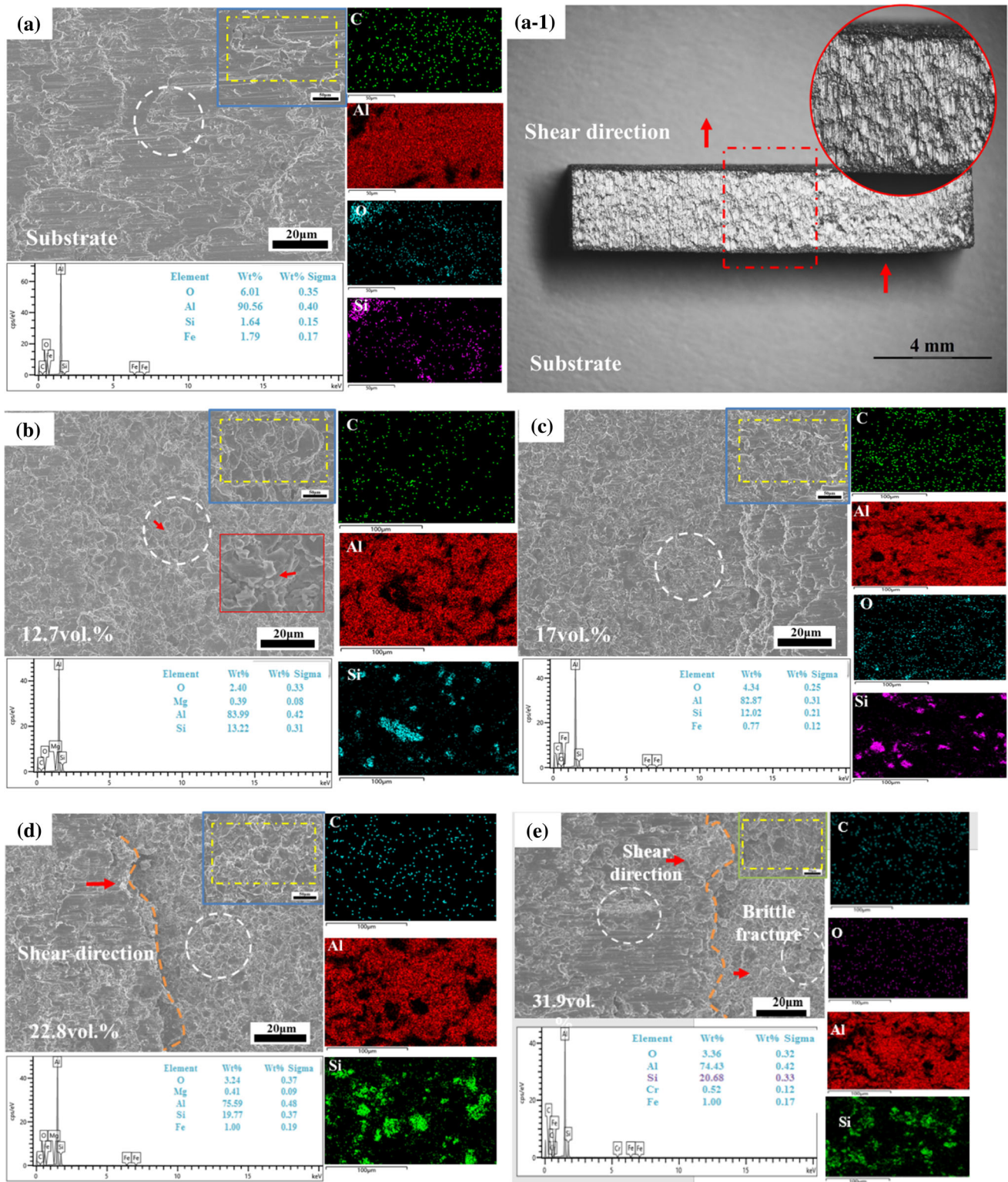
Fig. 11 Shear fracture morphologies of (a) Al substrate and the composite coatings of (b) Al5056/12.7 vol.%SiC, (c)Al5056/17 vol.%SiC, (d) Al5056/22.8 vol.%SiC and (e) Al5056/31.9 vol.%SiC

contributed to the X-ray diffraction method being very suitable for surface layers analysis of the composite coatings. Therefore, the measured residual stress in Fig. 13

could be a pre-deposition condition for the subsequent particles, which may determine its deposition behavior. A comparison of the residuals stress of the Al5056 composite

Fig. 12 Fitting plots of 2 $\theta_{\phi\psi}$-$sin^2\psi$ for cold-sprayed composite coatings of (a) Al5056+12.7 vol.%SiC, (b)Al5056+17 vol.%SiC, (c) Al5056+22.8 vol.%SiC and (d) Al5056+31.9 vol.%SiC
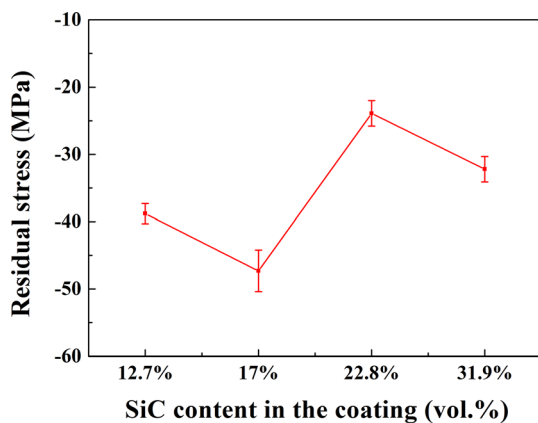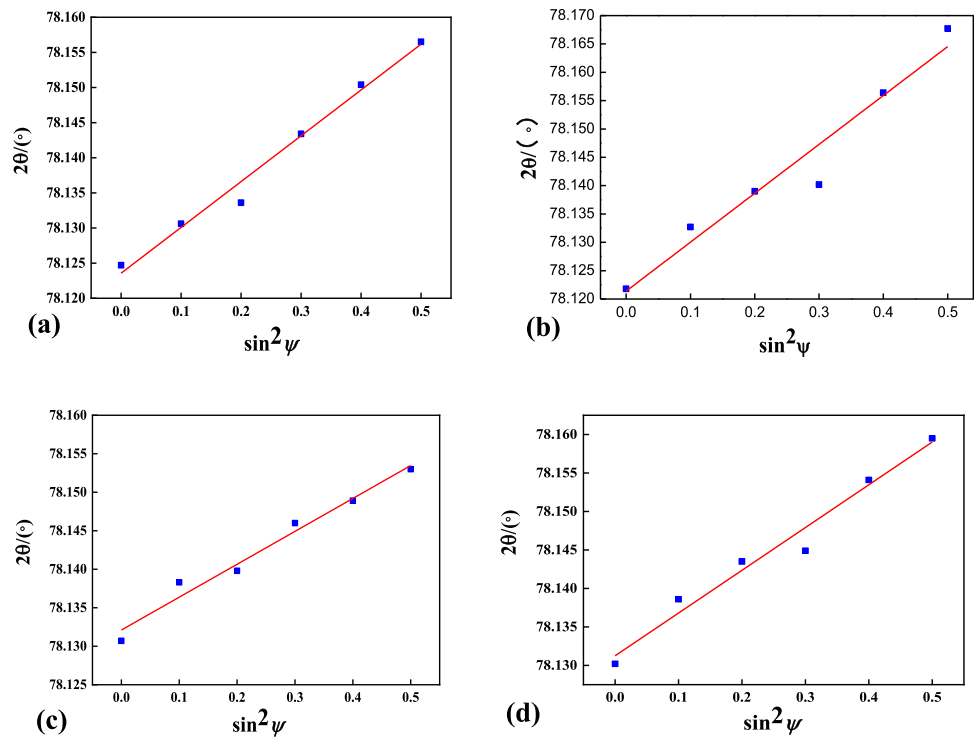
Fig. 13 Calculated residual stress by $sin^2\psi$ method

coating that was reinforced by 17 vol.% SiC with that reinforced by 12.7 vol.% SiC, showed that a 10 MPa increase in residual stress could be attributed to the peening effect of the additional 15 wt.% unbroken SiC in the powder. With a further increase in SiC content in the powder to 45 wt.%, the additional kinetic energy of the SiC particles dissipated as SiC fragmentation as shown in Fig.4(c), and thus, the peening effect of SiC on the deformed Al5056 particles decreased. The weakened peening and the presence of cracks in the SiC decrease the residual stress of the coating (Ref 35), which results in a decrease in surface residual stress of the Al5056 matrix. When the SiC broken threshold was surpassed, the SiC particles broke into a small size with a 31.9 vol.% content

retained in the coating and the Al5056 matrix was strengthened in a dispersed manner, which increased the residual stress of the Al5056 matrix.

The microstructure and mechanical property of the cold-sprayed Al5056\SiC composite coating depend on the co-deposition mechanism and co-reinforcement effect of the Al5056 and SiC particles. As mentioned in the experimental results, when the SiC content exceeded 40.3 vol.% in the powder, the SiC deposition efficiency increased significantly, that is, the 14 vol.% increase in the powder caused a 9 vol.% SiC increase in the Al5056/31.9 vol.% SiC coating compared with the Al5056/17 ~ 22.8 vol.% SiC composite coatings. The transition point occurred where the SiC broken threshold and the minimum residual stress were reached. Therefore, a bold speculation could be arisen that the lower compressive residual stress of the Al5056 particles favors SiC deposition in the coating.

Conclusions

(1) As the SiC content in the powder increased from 12.7 vol.% to 55.3 vol.%, the average SiC content in the coating increased from 12.7 vol.% to 31.9 vol.% and the SiC morphology in the coating evolved from completeness to complete fragmentation.

(2) The SiC distribution of the Al5056+17 vol.% SiC coating and the Al5056+12.7 vol.% SiC shows the best and worst uniformity, respectively, and the

smaller SiC powder has a positive effect on the uniform distribution in the composite coatings.

(3) The average coating microhardness increased from 108 to 133 HV as the SiC content in the coating increased from 12.7 vol.% to 31.9 vol.%. The increase in microhardness could mainly result from the SiC load sharing.

(4) Due to the SiC particle peening and fragmentation, the surface residual stress of the Al5056 matrix of the four composite coatings is -38.3 MPa, -47.3 MPa, -23.9 MPa and -32.2 MPa as the average SiC content in the coating increased from 12.7 vol.%, 17 vol.%, 22.8 vol. % to 31.9 vol.%.

References

1. A. Papyrin, V. Kosarev, S. Klinkov and A. Alkimov, *V, Fomin, Cold Spray Technology*, Elsevier, Oxford, U.K, 2006.

2. R.C. Dykhuizen and M.F. Smith, Gas Dynamic Principles of Cold Spray, *J. Therm. Spray Techn.*, 1998, **7**(2), p 205–212.

3. H. Assadi, H. Kreye, F. GaRtner and T. Klassen, Cold Spraying—A Materials Perspective, *Acta Mater.*, 2016, **116**, p 382–407.

4. V. Luzin, K. Spencer and M.-X. Zhang, Residual Stress and Thermo-Mechanical Properties of Cold Spray Metal Coatings, *Acta Mater.*, 2011, **59**(3), p 1259–1270.

5. W.B. Choi, L. Li, V. Luzin, R. Neiser, T. Gnaupel-Herold, H.J. Prask, S. Sampath and A. Gouldstone, Integrated Characterization of Cold Sprayed Aluminum Coatings, *Acta Mater.*, 2007, **55**(3), p 857–866.

6. V. Luzin, A. Valarezo and S. Sampath, Through-Thickness Residual Stress Measurement in Metal and Ceramic Spray Coatings by Neutron Diffraction, *Mater. Sci. Forum*, 2008, **571–572**, p 315–320.

7. G. Shayegan, H. Mahmoudi, R. Ghelichi, J. Villafuerte, J. Wang, M. Guagliano and H. Jahed, Residual stress induced by cold spray coating of magnesium AZ31B extrusion Mater, *Design*, 2014, **60**, p 72–84.

8. V.K. Champagne, The Repair of Magnesium Rotorcraft Components by Cold Spray, *J. Fail. Anal. Prev.*, 2008, **8**(2), p 164–175.

9. J.C. Lee, H.J. Kang, W.S. Chu and S.H. Ahn, Repair of Damaged Mold Surface by Cold-Spray Method, *CIRP Ann. Manuf. Techn.*, 2007, **56**(1), p 577–580.

10. M. Faccoli, G. Cornacchia, D. Maestrini, G.P. Marconi and R. Roberti, Cold Spray Repair of Martensitic Stainless Steel Components, *J. Therm. Spray Techn.*, 2014, **23**(8), p 1270–1280.

11. S. Grigoriev, A. Okunkova, A. Sova, P. Bertrand and I. Smurov, Cold Spraying: from Process Fundamentals Towards Advanced Applications, *Surf. Coat. Tech.*, 2016, **268**, p 77–84.

12. Y. Shuo, C. Pasquale, A. Barry, J. Richard, H.L. Liao, W.Y. Li and L. Rocco, Cold Spray Additive Manufacturing and Repair: Fundamentals And Applications, *Addit. Manuf.*, 2008, **21**, p 628–650.

13. W.Y. Li, Y. Kang, Y. Shuo, X.W. Yang, Y.X. Xu and R. Lupoi, Solid-State Additive Manufacturing and Repairing By Cold Spraying: A Review, *J. Mater. Sci. Technol.*, 2018, **34**(3), p 440–457.

14. C.J. Huang, Y.C. Xie, W.Y. Li, C. Verdy, M.P. Planche, H.L. Liao and G. Montacon, Advanced Brass-Based Composites Via Cold-Spray Additive-Manufacturing and its Potential In Component Repairing, *Surf. Coat. Tech.*, 2019, **371**, p 211–223.

15. E. Irissou, J.-G. Legoux, B. Arsenault and C. Moreau, Investigation of Al-Al₂O₃ Cold Spray Coating Formation and Properties, *J. Therm. Spray Techn.*, 2007, **16**(5–6), p 661–668.

16. W.Y. Li, G. Zhang, H.L. Liao and C. Coddet, Characterizations of Cold Sprayed TiN Particle Reinforced Al2319 Composite Coating, *J. Mater. Process. Tech.*, 2008, **202**(1–3), p 508–513.

17. E. Sansoucy, P. Marcoux, L. Ajdelsztajn and B. Jodoin, Properties of SiC-Reinforced Aluminum alloy Coatings Produced by the Cold Gas Dynamic Spraying Process, *Surf. Coat. Tech.*, 2008, **202**(16), p 3988–3996.

18. K. Spencer, D.M. Fabijanic and M.X. Zhang, The Use of Al-Al₂O₃ Cold Spray Coatings to Improve the surface properties of Magnesium Alloys, *Surf. Coat. Tech.*, 2009, **204**(3), p 336–344.

19. X.-T. Luo, G.-J. Yang and C.-J. Li, Multiple Strengthening Mechanisms of Cold-Sprayed cBNp/NiCrAl Composite Coating, *Surf. Coat. Tech.*, 2011, **205**(20), p 4808–4813.

20. F. Sevillano, P. Poza, C.J. Munez, S. Vezzu, S. Rech and A. Trentin, Cold-Sprayed Ni-Al₂ O₃ Coatings for Applications in Power Generation Industry, *J. Therm. Spray Techn.*, 2013, **22**(5), p 772–782.

21. M. Yu, X.K. Suo, W.Y. Li, Y.Y. Wang and H.L. Liao, Microstructure, Mechanical Property and Wear Performance of Cold Sprayed Al5056/SiCp Composite Coatings: Effect of Reinforcement Content, *Appl. Surf. Sci.*, 2014, **289**, p 188–196.

22. S.R. Bakshi, V. Singh, K. Balani, D.G. McCartney, S. Seal and A. Agarwal, Carbon Nanotube Reinforced Aluminum Composite Coating Via Cold Spraying, *Surf. Coat. Tech.*, 2008, **202**(21), p 5162–5169.

23. A. Shkodin, A. Kashirion, O. Kulyuev and T. Buzdygar, Metal Particle Deposition Stimulation by Surface Abrasive Treatment in Gas Dynamic Spraying, *J. Therm. Spray Techn.*, 2006, **15**(3), p 382–386.

24. Y. Tao, T. Xiong, C. Sun, H. Jin, H. Du and T. Li, Effect of α-Al₂O₃ on the Properties of Cold Sprayed Al/α-Al2O3 Composite Coatings on AZ91D Magnesium Alloy, *Appl. Surf. Sci.*, 2009, **256**(1), p 261–266.

25. Q. Wang, N. Birbilis, H. Huang and M.-X. Zhang, Microstructure Characterization and Nanomechanics of Cold-Sprayed Pure Al and Al-Al₂O₃ Composite Coatings, *Surf. Coat. Tech.*, 2013, **232**, p 216–223.

26. O. Meydanoglu, B. Jodoin and E.S. Kayali, Microstructure, Mechanical Properties and Corrosion Performance Of 7075 Al Matrix Ceramic Particle Reinforced Composite Coatings Produced by the Cold Gas Dynamic Spraying Process, *Surf. Coat. Tech.*, 2013, **235**, p 108–116.

27. J.M. Shockley, H.W. Strauss, R.R. Chromik, N. Brodusch, R. Gauvin, E. Irissou and J.G. Legoux, In Situ Tribometry of Cold-Sprayed Al-Al2o3 Composite Coatings, *Surf. Coat. Tech.*, 2013, **215**, p 350–356.

28. J.M. Shockley, S. Descartes, P. Vo, E. Irissou and R.R. Chromik, The Influence of Al₂O₃ Particle Morphology on the Coating Formation AND Dry Sliding Wear Behavior of Cold Sprayed Al-Al₂O₃ Composites, *Surf. Coat. Tech.*, 2015, **270**, p 324–333.

29. A. Sova, V.F. Kosarev, A. Papyrin and I. Smurov, Effect of Ceramic Particle Velocity on Cold Spray Deposition of Metal-Ceramic Coatings, *J. Therm. Spray Technol.*, 2010, **20**(1–2), p 285–291.

30. M. Yu, H. Chen, W.Y. Li, X.K. Suo and H.L. Liao, Building-Up Process of Cold-Sprayed Al5056/In718 Composite Coating, *J. Therm. Spray Techn.*, 2015, **24**(3), p 579–586.

31. T. Peat, A. Galloway, A. Toumpis and P. McNutt, N, Iqbal, The Erosion Performance of Particle Reinforced Metal Matrix Composite Coatings Produced by Co-Deposition Cold Gas Dynamic Spraying, *Appl. Surf. Sci.*, 2017, **396**, p 1623–1634.

32. S.B. Prabu, L. Karunamoorthy, S. Kathiresan and B. Mohan, Influence of Stirring Speed and Stirring Time on Distribution of Particles in Cast Metal Matrix Composite, *J. Mater. Process. Tech.*, 2006, **171**(2), p 268–273.

33. A. Slipenyuk, V. Kuprin, Y. Milman, J.E. Spowart and D.B. Miracle, The Effect of Matrix to Reinforcement Particle Size Ratio (PSR) on the Microstructure and Mechanical Properties of a P/M Processed AlCuMn/SiCp MMC, *Mat. Sci. Eng. A-Struct.*, 2004, **381**(1–2), p 165–170.

34. K. Cao, M. Yu, C.M. Liang, H. Chen, Quantitative determination of SiC particles distribution of cold sprayed Al5056/SiC composite coatings, *Surf. Eng.*, https://doi.org/10.1080/02670844.2019.1609741

35. P.C. King, S.H. Zahiri and M. Jahedi, Focused Ion Beam Micro-Dissection of Cold-Sprayed Particles, *Acta Mater.*, 2008, **56**, p 5617–5626.

36. K.D. Bouzakis and N. Michailidis, Coating Elastic-Plastic Properties Determined By Means of Nanoindentations and FEM-Supported Evaluation Algorithms, *Thin Solid Films*, 2004, **469**, p 227–232.

37. K. Spencer, V. Luzin, N. Matthews and M.-X. Zhang, Residual Stresses in Cold Spray Al Coatings: The Effect of Alloying and of Process Parameters, *Surf. Coat. Tech.*, 2012, **206**(s19–20), p 4249–4255.

38. R. Sinclair-Adamson, V. Luzin, A. Duguid, K. Kannoorpatti and R. Murray, Residual Stress Distributions in Cold-Sprayed Copper 3d-Printed Parts, *J. Therm. Spray Techn.*, 2020, **29**(3), p 1525–1537.

Publisher's Note Springer Nature remains neutral with regard to jurisdictional claims in published maps and institutional affiliations.